Nanoscale

Nanoscale

www.rsc.org/nanoscale

ROYAL SOCIETY
OF CHEMISTRY

ROYAL SOCIETY
OF CHEMISTRY

www.rsc.org/nanoscale

Nanoscale

ARTICLE

Visible Light Response, Electrical Transport, and Amorphization in compressed Organolead Iodine Perovskite

Tianji Ou[a], Jiejuan Yan[a], Chuanhai Xiao[a], Wenshu Shen[a], Cailong Liu*[a], Xizhe Liu[a], Yonghao Han[a], Yanzhang Ma[b], and Chunxiao Gao*[a]

Recent scientific advances on the organic-inorganic hybrid perovskites are mainly focused on the improvement of power conversion efficiency. So far, how compression tunes their electronic and structural properties remain less understood. By combing *in situ* photocurrent, impedance spectroscopy, and X-ray diffraction (XRD) measurements, we have studied the electrical transport and structural properties of compressed $CH_3NH_3PbI_3$ ($MAPbI_3$) nanorods. The visible light response of $MAPbI_3$ keeps robust below 3 GPa while is suppressed when it becomes amorphous. Pressure-induced electrical transport properties of $MAPbI_3$ including resistance, relaxation frequency, and relative permittivity have been investigated under pressure up to 8.5 GPa by *in situ* impedance spectroscopy measurements. These results indicate that the discontinuous changes of these physical parameters occur around the structural phase transition pressure. The XRD studies of $MAPbI_3$ under high pressure up to 20.9 GPa show that a phase transformation below 0.7 GPa, which could be attributed to the tilting and distortionof PbI_6 octahedra. And pressure-induced amorphization is reversible at low density amorphous state but irreversible at relative higher density state. Furthermore, the $MAPbI_3$ nanorods crush into nano pieces around 0.9 GPa which help us explain why the mixed phase of tetragonal and orthorhombic was observed at 0.5 GPa. The pressure modulated changes of electrical transport and visible light response properties open up a new approach for exploring $CH_3NH_3PbI_3$-based photo-electronic applications.

Introduction

Recently, the organic-inorganic hybrid perovskites, $CH_3NH_3PbI_3$ ($MAPbI_3$) have attracted extensive scientific interest as light-harvesting materials for solar conversion applications owing to their direct band-gap with large absorption coefficient, high carrier mobility, and long electron-hole diffusion length and low-cost.[1-5] Since the first report by Kojima *et al.* used $MAPbI_3$ as sensitizing materials in liquid dye-sensitized solar cells (DSCs) in 2009, with a very low power conversion efficiency (PCE) of 3.8%,[1] the PCE of $MAPbI_3$-based photovoltaic devices has been improved up to ~20%,[2, 3, 6-10] which is comparable with those of the commercial silicon solar cells. In fact, it is the good optical absorption characteristic and better charge transport properties that render $MAPbI_3$ as a highly efficient light harvester.[5, 6, 11-13] Despite the rapid progress in improving the solar cell performance, the electronic and charge transport properties of $MAPbI_3$ is still less understood, which hampers the prospects for further improvement of conversion efficiency of $MAPbI_3$-based electronic devices.

Pioneering studies revealed that $MAPbI_3$ shows strong absorbance in the visible wavelength range with a direct energy band gap of around 1.5 eV,[8] and its electronic structure was sensitive to external conditions, e.g. temperature, chemical component, and pressure.[10, 14-18] On the one hand, the electronic structure of $MAPbI_3$, including its energy band-gap can be tuned significantly on cooling process accompanied with the cubic-tetragonal-orthorhombic structural transitions.[15, 19, 20] On the other hand, the band gap and absorbance spectra of perovskites can also be adjusted by changing the ratio of the halide in perovskite, i.e. $MAPb(I_{1-x}Br_x)_3$, $MAPbI_{3-x}Cl_x$.[10, 17] As well known, compression is a powerful tool to drive transformation toward the structures with higher density without inducing impurity, and hence modulates the electronic structure of materials.[21] Recently, Zhao *et al.* have studied the optical and structural properties of $MAPbBr_3$ under compression, and found that the electronic structure can be tuned obviously by applying pressure.[22] Moreover, the considerable effect of hydrostatic pressure and temperature on crystal structural stability and dielectric properties were also observed on single crystal $MAPbI_3$.[14, 16, 18] Nevertheless, the electrical transport property of $MAPbI_3$ under compression is still rarely studied. More importantly, in the recent researches, Hu *et al.*[23] have fabricated the photodetectors based on $MAPbI_3$ film which has a broad photoresponse range from 780 *nm* to 310 *nm*, far exceeding the performance of current photodetectors. And zhuo *et al.*[24]

a. State Key Laboratory of Superhard Materials, Institute of Atomic and Molecular Physics, Jilin University, Changchun 130012, China. E-mail: cailong_liu@jlu.edu.cn, cc060109@qq.com
b. Department of Mechanical Engineering, Texas Tech University, Lubbock, Texas 79409, USA

have reported that the porous MAPbBr$_3$ nanowires exhibit superior promising optoelectronic performance. It remains unclear how compression tunes the visible-light response of MAPbI$_3$, one of important characteristics used for electronic devices. Besides, it was found that, in polycrystalline semiconductor absorbers, grain boundaries can heavily affect the electrical transport properties and consequently the performance of solar cells due to the increased free carrier scattering effect at grain boundaries.[25-28] However, the effect of grain boundary on the electrical transport properties of MAPbI$_3$ under compression is under investigated and thus poorly understood.

Activated by the above mentioned issues, we conducted the high-pressure photocurrent measurements to explore the effect of compression on visible light response of MAPbI$_3$. The alternating current (AC) impedance spectroscopy measurements were used to study pressure-induced variations on the electrical transport properties and grain boundary effect of MAPbI$_3$, by which the contribution of bulk and grain boundaries can be distinguished clearly. In addition, *in situ* high-pressure XRD measurements were conducted to monitor the structural modification under compression, which is great importance for understanding the changes of physical properties of MAPbI$_3$. By combing these measurements, we found that the visible light response of MAPbI$_3$ keeps robust below 3 GPa while is suppressed when it becomes amorphous. The electrical transport properties of MAPbI$_3$ changed anomalously at ~0.6 GPa, followed with the tetragonal to orthorhombic structural transition.

Experiments

MAPbI$_3$ nanorods were synthesized by coprecipitation method using spin coating technique, based on the procedure reported previously,[29] The details of the sample synthesis and handling can be found in the supporting information. Both the sample storage and sample loading processes were carried out in an argon-filled glovebox.

Diamond anvil cell (DAC) with culet of 400 μm in diameter was utilized to generate high pressure. The quasi-four-point-probe was located on surface of one of diamond anvils in our high pressure *in situ* photocurrent measurements which can be found in ref (22). The AC impedance spectroscopy measurements were performed by the plate electrodes with one Mo film electrode integrated on one diamond surface and the other on the faced diamond. The detailed integration process of Mo film electrodes has been reported previously.[30] A T301 stainless steel was pre-indented into 60 μm in thickness, and then a hole of 250 μm in diameter was drilled at the centre of indentation by laser drilling machine. Then, a mixture of cubic boron nitride powder and epoxy was compressed into the indentation, as the insulating layer. Subsequently, another hole of 150 μm was drilled and served as a sample chamber. Pressure was calibrated by R1 fluorescence peak of ruby.[31] No pressure-transmitting medium was used to avoid additional error on the electrical transport measurements. The thickness of sample under pressure was

determined by micrometer with precision of 0.5 μm, and the deformation of diamond anvils was taken into account.[32] The impedance spectroscopy was measured by a Solartron 1260 impedance analyser equipped with Solartron 1296 dielectric interface. Sine signal with amplitude of 1 V and frequency ranged from 0.1 to 10^7 Hz was applied into the sample.

In situ high-pressure XRD measurements were conducted at beamline 4W2 of Beijing Synchrotron Radiation Facility (BSRF) and BL15U1 of Shanghai Synchrotron Radiation Facility (SSRF) using angle-dispersive XRD source (λ = 0.6199 Å). No pressure-transmitting medium was loaded in Run 1 for better comparison with electrical transport properties. Silicone oil was used as the pressure transmitting medium in Run 2. Distance between sample and detector, and parameters of detector were calibrated using a CeO$_2$ standard. Bragg diffraction images were integrated using Fit2d software, yielding one-dimensional intensity versus diffraction angle 2θ patterns.

Scanning electron microscopy (SEM) images were obtained *via* a FEI MAGELLAN-400 microscope. High resolution transmission electron microscopy (HRTEM) images were obtained on a JEM-2200FS transmission electron microscope using an accelerating voltage of 200 kV.

Results and Discussion

The MAPbI$_3$ samples synthesized in our experiments crystallizes into tetragonal structure with space group *I4/mcm* and lattice constants of a= 8.8743(4) Å, c=12.6708(5) Å, agreeing well with the previously reported results.[33] Shown in Fig. 1 is the Scanning Electronic Microscopy (SEM) image of MAPbI$_3$. The dimension of the MAPbI$_3$ nanorods is 0.5 ~ 0.6 μm in length and 80 ~ 100 nm in diameter on average.

The photocurrent and electrical parameters are important characteristics used for application of electronic devices. We carried out photocurrent measurements on MAPbI$_3$ to make *in situ* observation of the pressure effect on visible light response. The time-dependent photocurrent was recorded
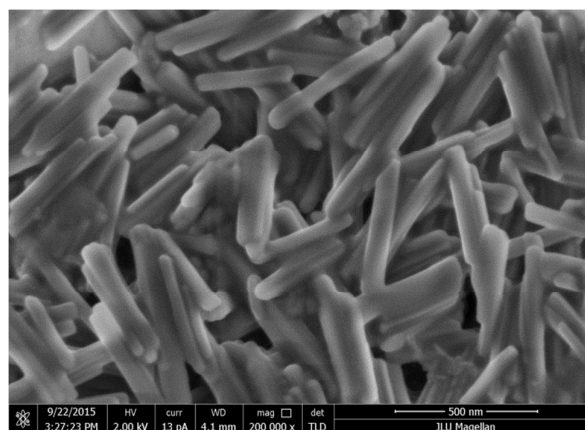

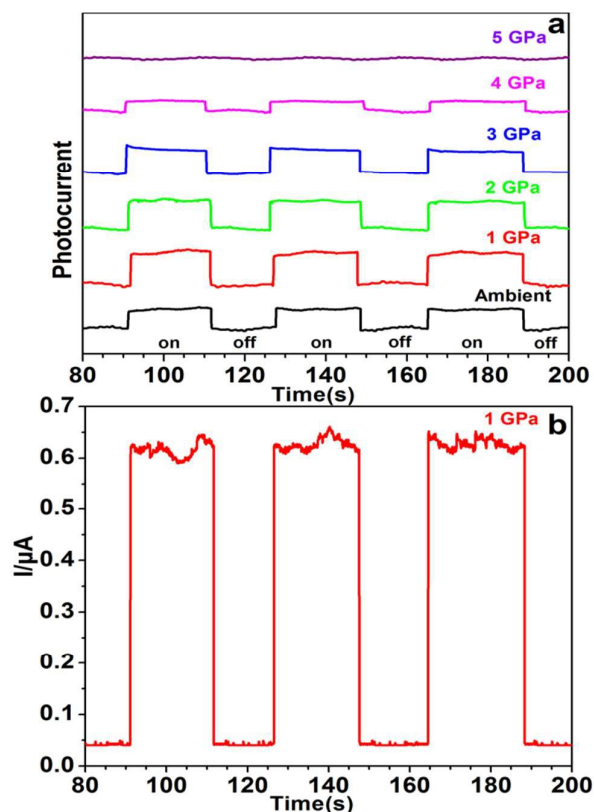Figure 1. SEM images of the MAPbI$_3$ nanorods.

Figure 2. (a) Photocurrent of MAPbI$_3$ as a function of pressure. (b) The detailed response of photocurrent at 1 GPa.

when the white light (2W·cm^{-2}) was turned on and off repeatedly. Fig. 2a and 2b illustrate the pressure-induced variations of photocurrent when the device was applied to a constant Voltage U=5 V. It is found that the photocurrent increased sharply as the light turned on and then dropped rapidly to the original value when the light was turned off, indicating a good optoelectronic character. The photocurrent response keeps robust in the low pressure region (<3 GPa). However, with further compression up to 4 GPa, the photocurrent of sample decreased significantly and almost disappeared above 5 GPa. The specific pressure independent photocurrent values are shown in Fig. S1.

To gain deeper insight into the effect of pressure on the electrical properties and grain boundaries of MAPbI$_3$, we conducted *in situ* high-pressure AC impedance spectroscopy measurements, by which the electrical transport parameters of MAPbI$_3$ including bulk and grain boundaries resistances, relaxation frequencies, and relative permittivity can be extracted distinctly. Shown in Fig. 3a and 3b are the Nyquist plots of the impedance spectra of MAPbI$_3$ with pressure up to 8.5 GPa. It is found that, unlike previously reported impedance spectra observations where two semicircles describing the bulk and boundary effect can be distinguished clearly in the complex plane,[34] only one semicircle describing the bulk contribution can be observed on the impedance spectra results of MAPbI$_3$.The components represented to the grain boundary and contact effect between sample and film

electrodes (several ohms) are too weaker compared with those of the bulk contribution to distinguish them clearly. That is why the bulk conduction process dominates the electrical transport behaviour of MAPbI$_3$, which is extremely desirable for MAPbI$_3$-based electronic devices. Recently reported photoluminescence measurements[35] and theoretical research results[25] also support our observations that there is very weak contribution of the grain boundary to the electrical transportation process of MAPbI$_3$. With increasing pressure up to 0.6 GPa, impedance spectra comprise a single semicircle whose diameter decreases when pressure increases. We note that, above 0.6 GPa, the semicircles tend to broaden with pressure increasing especially the pressure exceed 4.4 GPa. The pressure-dependent total resistances of MAPbI$_3$ are shown in Fig. 3c. According to the variation trends of the pressure-dependent resistances, the pressures are assigned into three regions as I, II, and III.

In addition, from the impedance spectra data, we can gain the dielectric properties of MAPbI$_3$ under compression. With the parallel-plate electrode model, the relative permittivity (ε_r) of the grains as a function of pressure can be obtained according to the following formula:

$$\varepsilon_r(p) = (d/2\pi R f \varepsilon_o S)$$

Where d, S, ε_o, R, and f is the thickness of samples, contacted area electrodes, vacuum permittivity, and resistances relaxation frequency of grains, respectively. Fig. 3d and 3e show the pressure dependence of relative permittivity and relaxation frequencies of MAPbI$_3$, respectively. Because the bulk conduction process dominates the electrical transport behaviour of MAPbI$_3$, it is reasonable to conclude that the dielectric properties of MAPbI$_3$ under pressure are determined by the grain's interior transport process. Under compression, it is found that different variation trends in both the pressure-dependent relative permittivity and relaxation frequencies can
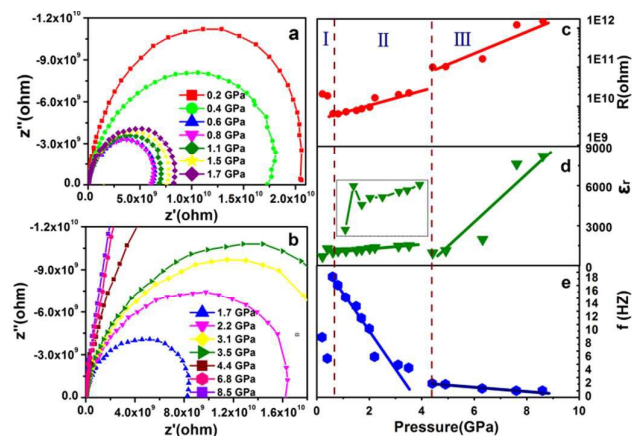

Figure 3. The Nyquist plot of complex impedance planes of MAPbI$_3$ at different pressures: (a) 0.2~1.7 GPa (b) 1.7~8.5 GPa. The pressure-dependent electrical transportation parameters of MAPbI$_3$: (c) resistance, (d) relative permittivity, and (e) relaxation frequency. The insert in panel (d) further displays the pressure-dependent relative permittivity from ambient to 2 GPa.

be observed at different pressure regions.

In fact, most anomalies of the electrical parameters are usually coincided with crystal structure transition.[36, 37] *In situ* high pressure XRD experiments were conducted to monitor the structural modification of MAPbI$_3$ under compression. The Run 1 is shown in Fig. 4. Fig. 4a shows two-dimensional raw XRD images at five selected pressures during compression. With increasing pressure, some sharp rings become weaker along with the appearance of others new broad peaks, indicating the I-II structural transition. Above 11.5 GPa, almost all of the initial diffraction rings disappear and only two broad rings remain, which clearly signals that the amorphous character of MAPbI$_3$. Fig. 4b illustrates the integrated XRD patterns of MAPbI$_3$ up to 20.9 GPa. At ambient conditions, MAPbI$_3$ crystallizes into tetragonal structure with *I4/mcm* symmetry. With gradually increasing pressure up to 0.7 GPa, two new peaks at ~9.0°, 10.8° emerges suddenly, followed by the disappearance of the (211) peak in phase I. During the preparation of this manuscript, we became aware of an arXiv paper that reported by Kai Wang *et al.*. Compatible with their results, the phase II can be well indexed into orthorhombic structure. The XRD pattern at 0.5 GPa means the coexistence of both the tetragonal and orthorhombic structure. The patterns of phase II can be well indexed into orthorhombic structure. The XRD pattern at 0.5 GPa means the coexistence

Figure 4. XRD patterns collected at various pressures for MAPbI$_3$ during compression and decompression: (a) The raw 2D XRD images and (b) integrated 1D XRD profiles

of both the tetragonal and orthorhombic structure. Above 0.7 GPa, with continuous increasing of pressure, there is no obvious variation on the patterns of MAPbI$_3$ except the relative peak broadening and the collective movements of all reflection peaks toward lower d-spacing. When the applied pressure is bigger than 4.2 GPa, the sample start to be partly amorphous, which lead to the anomalous electrical transportation parameters variations in region III (Fig. 3). When the applied pressure exceeds 11.5 GPa, all the diffraction peaks lose their intensity, indicating that MAPbI$_3$ becomes amorphous. After quenching to ambient pressure, all of the reflection peaks of the tetragonal phase re-emerged (Fig. 4b), indicating that the amorphization process is reversible. However, it is found that when the sample is pressurized up to 20.9 GPa and then quenched to ambient pressure, the pattern remains disappeared, showing the irreversible character. This type of structural transition is because of the titling and distortion of PbI$_6$ under compression. The reversible character can be attributed to that the flexible organic cations act as templates for the P-I frameworks according to the Raman measurement results. The irreversible character is due to the breaking and unrecoverable of P-I frameworks.

In Kai Wang *et al.*'s reports, the phase transformation from the tetragonal to orthorhombic in bulk MAPbI$_3$ samples is at ~ 0.3 GPa. They use argon, silicon oil, and KrBr as the pressure medium which provide a nearly hydrostatic condition in the sample chamber. However, in our Run 1, due to no pressure medium was loaded which get a non-hydrostatic condition in the sample chamber, this explained why a mixed phase of tetragonal and orthorhombic was observed at 0.5 GPa and the structural transition finished at ~ 0.7 GPa. In Run 2, (Figure S2) silicone oil was used as the pressure transmitting medium, there were no mixed phase states can be observed during the entire phase transition process, and the structural transition also finished at ~0.3 GPa. This means no clearly size effects were observed between our nanorods and Wang *et al.*'s bulk material under compression.

As well known, even the same structural material with different surface and interfaces, both size effect[38] and interface effect[39] can result in the different structural transition pressure and even the structural transition pathways. Thus, it is necessary to try to characterize the *in situ* surface and interface properties of MAPbI$_3$ under compression. Thus far, there is no way to characterize the *in situ* morphology under compression because of experimental restrictions. Here, in order to reflect to surface and interface properties indirectly, HRTEM was used to get the images of MAPbI$_3$ samples after decompression from 0.3, 0.6, and 0.9 GPa, respectively as shown in Fig. 5. At 0.3 GPa (Fig. 5a) and 0.6 GPa (Fig. 5b), the MAPbI$_3$ samples still keep their nanorods character. With increasing the pressure up to 0.9 GPa, the nanorods can't be observed anymore, instead the samples was compressed into a compact one (Fig. 5c). Through HRTEM image of the decompressed sample as shown in Fig. 5d, some nanodomains which exhibit short range order was observed. The average sample size changed from 0.5~0.6 μm in length and 80~100 nm in diameter to arbitrary shapes with the size of ~ 10 nm at 0.9
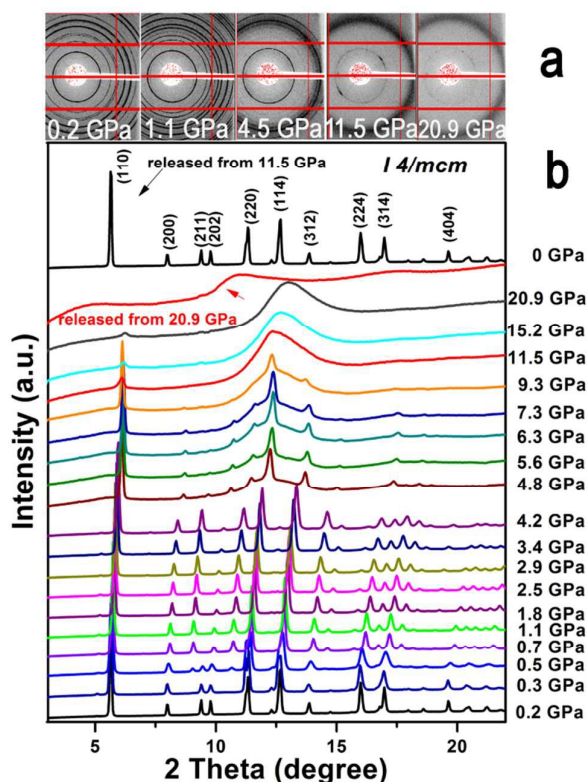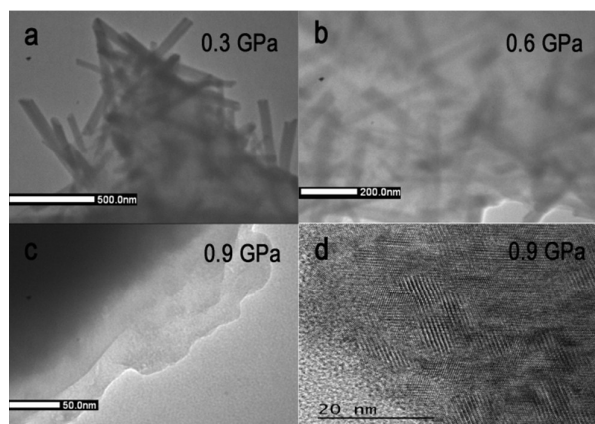
Figure 5. TEM images of the MAPbI$_3$ samples after decompression from different pressures. (a) 0.3 GPa; (b) 0.6 GPa; (c) 0.9 GPa. (d) HRTEM images at 0.9 GPa.

GPa. Compared with the pressure-induced nanocrystalization pressure in some inorganic materials (12.5 GPa in ZnSnO$_4$,[39] 15 GPa in Cu$_2$O,[40] 11 GPa in Alq$_3$.[41]), 0.9 GPa is very low, which means the MAPbI$_3$ samples belong to the class of soft materials. The deviatoric stress in the MAPbI$_3$ sample chamber makes a non-hydrostatic condition before 0.9 GPa because of the nanorods character. Before the nanorods crush into nano pieces the deviatoric stress still big enough to lead to the appearance of the mixed phase of tetragonal and orthorhombic at 0.5 GPa.

It should be noticed that the resistance has a drop from ambient to 0.6 GPa. Two factors are related to this drop. As nanorods were filled into the cell, a lot of gaps with big resistance remained among nanorods. With increasing pressure, the density of the gaps decreased quickly and caused a rapid decrease in resistance.[40] Meanwhile, pressure induced band gap shrink which may lead to a decrease in resistance. From 0.6 to 4.4 GPa (Fig. 3c), the resistance turns to increase with pressure increasing, this because at this pressure section, the crystal adopts an orthorhombic structure, in which the PbI$_6$ octahedral are strongly deformed assuming a rectangular basal plane. Such deformation restricts the rotational degrees of freedom of CH$_3$NH$_3$ in the rhombus-shaped interstitial region, thus imposing a spatial ordering to CH$_3$NH$_3$.[42] As pressure was increased, the interaction between the organic molecules and the inorganic framework driven by the dispersive forces enhanced. As a result, the CH$_3$NH$_3$ exerts strain on the PbI$_6$ octahedra and leads to the increase of band gap and the total electrical resistance. Below 3 GPa, the electrical resistance value changes in MAPbI3 are less than one order of magnitude (can be seen in Fig. 3c), corresponding to the photocurrents show negligible changes under the pressure lower than 3 GPa. As can be seen from XRD results in Fig. 4b, the sample began to amorphous above 4.2 GPa. This may be the reason of the increases of the total resistance, relative permittivity, and the decreases of the relaxation frequency under compression above 4.4 GPa. The amorphization can also help us to understand why the photocurrent got weaker and almost disappeared at 5 GPa.

Conclusions

By high pressure *in situ* photocurrent, impedance spectroscopy, and XRD measurements, we have studied the electrical transport and structural properties of MAPbI$_3$ nanorods. The experimental results reveal that the electrical transport parameters, including resistance, relaxation frequency, and relative permittivity of MAPbI$_3$ change anomalously at ~0.6 GPa, followed with the tetragonal to orthorhombic structural transition, which can be attributed to the tilting and distortion of PbI$_6$ octahedra under compression that results in the broadening of the energy band-gap. The grain boundary effect and contact effect between sample and Mo film electrodes was found much weaker compared with those of the bulk contribution. Through the HRTEM data of the sample after decompression, the pressure-induced nanorods crush behaviour was observed at 0.9 GPa which verify this material belong to a class of soft material. The non-hydrostatic conditions in the chamber lead to observation of mixed phase of tetragonal and orthorhombic at 0.5 GPa. The visible light response of MAPbI$_3$ keeps robust below 3 GPa while is suppressed when MAPbI$_3$ become amorphous. The pressure modulated changes of electrical transport and visible light response properties open up a new approach for exploring CH$_3$NH$_3$PbI$_3$-based photo-electronic applications.

Acknowledgements

Notes and references

1. A. Kojima, K. Teshima, Y. Shirai and T. Miyasaka, *J. Am. Chem. Soc.* 2009, **131**, 6050.
2. N. G. Park, *J. Phys. Chem. Lett.*, 2013, **4**, 2423-2429.
3. J. Burschka, N. Pellet, S. J. Moon, R. Humphry-Baker, P. Gao, M. K. Nazeeruddin and M. Gratzel, *Nature*, 2013, **499**, 316-319.
4. M. Liu, M. B. Johnston and H. J. Snaith, *Nature*, 2013, **501**, 395-398.
5. G. Xing, N. Mathews, S. Sun, S. S. Lim, Y. M. Lam, M. Gratzel, S. Mhaisalkar and T. C. Sum, *Science*, 2013, **342**, 344-347.
6. J. H. Im, C. R. Lee, J. W. Lee, S. W. Park and N. G. Park, *Nanoscale*, 2011, **3**, 4088-4093.
7. L. Etgar, P. Gao, Z. Xue, Q. Peng, A. K. Chandiran, B. Liu, M. K. Nazeeruddin and M. Gratzel, *J. Am. Chem. Soc.*, 2012, **134**, 17396-17399.
8. H. S. Kim, C. R. Lee, J. H. Im, K. B. Lee, T. Moehl, A. Marchioro, S. J. Moon, R. Humphry-Baker, J. H. Yum, J. E. Moser, M. Gratzel and N. G. Park, *Sci Rep*, 2012, **2**, 591.
9. M. M. Lee, J. Teuscher, T. Miyasaka, T. N. Murakami and H. J. Snaith, *Science*, 2012, **338**, 643-647.
10. J. H. Noh, S. H. Im, J. H. Heo, T. N. Mandal and S. I. Seok, *Nano letters*, 2013, **13**, 1764-1769.
11. S. D. Stranks, G. E. Eperon, G. Grancini, C. Menelaou, M. J.

Alcocer, T. Leijtens, L. M. Herz, A. Petrozza and H. J. Snaith, *Science*, 2013, **342**, 341-344.

12. T. C. Sum and N. Mathews, *Energy Environ. Sci.*, 2014, **7**, 2518-2534.

13. G. E. Eperon, S. D. Stranks, C. Menelaou, M. B. Johnston, L. M. Herz and H. J. Snaith, *Energy Environ. Sci.*, 2014, **7**, 982.

14. N. ONODA-YAMAMURO, T. MATSUO and H. SUGA, *J. Phys. Chem. Solids*, 1992, **53**, 935-939.

15. A. Poglitsch and D. Weber, *J. Chem. Phys.*, 1987, **87**, 6373.

16. K. Gesi, *Ferroelectrics*, 1997, **203**, 249-268.

17. S. Colella, E. Mosconi, P. Fedeli, A. Listorti, F. Gazza, F. Orlandi, P. Ferro, T. Besagni, A. Rizzo, G. Calestani, G. Gigli, F. De Angelis and R. Mosca, *Chem. Mater.*, 2013, **25**, 4613-4618.

18. N. ONODA-YAMAMURO, O. YAMAMURO, T. MATSUO and H. SUGA, *J. Phys. Chem. Solids*, 1992, **53**, 277-281,.

19. D. Weber, *Z. Naturforsch.* , 1978, **33 b**, 1443-1445.

20. R. E. Wasylishen, O. Knop and J. B. Macdonald, *Solid State Commun.*, 1985, **56**, 581-582.

21. P. Dera, C. T. Prewitt, S. Japel, D. L. Bish and C. T. Johnston, *Am Mineral*, 2003, **88**, 1428-1435.

22. Y. Wang, X. Lu, W. Yang, T. Wen, L. Yang, X. Ren, L. Wang, Z. Lin and Y. Zhao, *J. Am. Chem. Soc.*, 2015, **137**, 11144-11149.

23. X. Hu, X. Zhang, L. Liang, J. Bao, S. Li, W. Yang and Y. Xie, *Adv. Funct. Mater.*, 2014, **24**, 7373-7380.

24. S. Zhuo, J. Zhang, Y. Shi, Y. Huang and B. Zhang, *Angew. Chem.*, 2015, **54**, 5693-5696.

25. W. J. Yin, T. Shi and Y. Yan, *Adv. Mater.*, 2014, **26**, 4653-4658.

26. L. X. Zhang, J. L. F. Da Silva, J. B. Li, Y. F. Yan, T. A. Gessert and S. H. Wei, *Phys. Rev. Lett.*, 2008, **101**.155501

27. W.-J. Yin, Y. Wu, S.-H. Wei, R. Noufi, M. M. Al-Jassim and Y. Yan, *Adv. Energy Mater.*, 2014, **4**, 1300712

28. D. Abou-Ras, S. S. Schmidt, R. Caballero, T. Unold, H. W. Schock, C. T. Koch, B. Schaffer, M. Schaffer, P. P. Choi and O. Cojocaru-Miredin, *Adv. Energy Mater.* 2012, **2**, 992-998.

29. N. Rajamanickam, S. Rajashabala and K. Ramachandran, *AIP Conf. Proc.*, 2015, **1665**.080034

30. M. Li, C. X. Gao, Y. Z. Ma, Y. C. Li, X. D. Li, H. Li, J. Liu, A. M. Hao, C. Y. He, X. W. Huang, D. M. Zhang and C. L. Yu, *Rev. Sci. Instrum.*, 2006, **77**.123902

31. H. K. Mao, P. M. Bell, J. W. Shaner and D. J. Steinberg, *J.Appl.Phys.* 1978, **49**, 3276.

32. M. Li, C. X. Gao, G. Peng, C. Y. He, A. M. Hao, X. W. Huang, D. M. Zhang, C. L. Yu, Y. Z. Ma and G. T. Zou, *Rev Sci Instrum*, 2007, **78**.075106

33. T. Baikie, Y. Fang, J. M. Kadro, M. Schreyer, F. Wei, S. G. Mhaisalkar, M. Graetzel and T. J. White, *J. Mater. Chem. A*, 2013, **1**, 5628.

34. C. Y. He, C. X. Gao, Y. Z. Ma, M. Li, A. M. Hao, X. W. Huang, B. G. Liu, D. M. Zhang, C. L. Yu, G. T. Zou, Y. C. Li, H. Li, X. D. Li and J. Liu, *Appl.Phys.Lett.*, 2007, **91**.092124

35. D. W. deQuilettes, S. M. Vorpahl, S. D. Stranks, H. Nagaoka, G. E. Eperon, M. E. Ziffer, H. J. Snaith and D. S. Ginger, *Science*, 2015, **348**, 683-686.

36. Y. H. Han, C. X. Gao, Y. Z. Ma, H. W. Liu, Y. W. Pan, J. F. Luo, M. Li, C. Y. He, X. W. Huang and G. T. Zou, *Appl. Phys. Lett.*, 2005, **86**.064104

37. C. L. Yu, Q. J. Yu, C. X. Gao, H. B. Yang, B. Liu, G. Peng, Y. H. Han, D. M. Zhang, X. Y. Cui, C. L. Liu, Y. Wang, B. J. Wu, C. Y. He, X. W. Huang and G. T. Zou, *J. Appl. Phys.*, 2008, **103**.114901

38. L. Wang, W. G. Yang, Y. Ding, Y. Ren, S. G. Xiao, B. B. Liu, S. V. Sinogeikin, Y. Meng, D. J. Gosztola, G. Y. Shen, R. J. Hemley, W. L. Mao and H. K. Mao, *Phys. Rev. Lett.*, 2010, **105**.095701

39. H. W. Zhang, F. Ke, Y. Li, L. Wang, C. L. Liu, Y. Zeng, M. G. Yao, Y. H. Han, Y. Z. Ma and C. X. Gao, *Sci Rep-Uk*, 2015, **5**.41359-41364

40. C. L. Liu, Y. M. Sui, W. B. Ren, B. H. Ma, Y. Li, N. N. Su, Q. L. Wang, Y. Q. Li, J. K. Zhang, Y. H. Han, Y. Z. Ma and C. X. Gao, *Inorg.chem.*, 2012, **51**, 7001-7003.

41. F. Ke, Q. L. Wang, J. K. Zhang, Y. Guo, D. Y. Tan, Y. Li, C. L. Liu, Y. H. Han, Y. Z. Ma, X. J. Chen, B. Chen and C. X. Gao, *Rsc Adv.*, 2015, **5**, 41359-41364.

42. C. Motta, F. El-Mellouhi, S. Kais, N. Tabet, F. Alharbi and S. Sanvito, *Nat. Commun.*, 2015, **6**.7026